Proceedings of the 2nd International Conference on Fluid Flow, Heat and Mass Transfer
Ottawa, Ontario, Canada, April 30 – May 1, 2015
Paper No. 154

Datailed-Chemistry Modeling of a Bluff-Body Stabilized Methanol/Air Turbulent Nonpremixed Flame Using Finite-Element-Volume Method

Masoud Darbandi, Majid Ghafourizadeh
Department of Aerospace Engineering,
Centre of Excellence in Aerospace Systems,
Sharif University of Technology, Tehran, P.O. Box 11365-8639, Iran
darbandi@sharif.edu; majid.ghafourizadeh@gmail.com

Gerry E. Schneider
Department of Mechanical and Mechatronics Engineering,
University of Waterloo, Waterloo, Ontario, N2L 3G1, Canada
gerry.schneider@uwaterloo.ca

Abstract- A gaseous-methanol/air turbulent nonpremixed flame stabilized on an axisymmetric bluff-body burner, i.e. an O-ring-type flame holder, is simulated using a hybrid finite-element-volume FEV method. We use a chemical mechanism consisting of 70 species and 463 elementary reactions for detail-chemistry calculations of the flame and adopt flamelet combustion model to surmount the closure problem of chemical source terms within the classical Reynolds-Stress-Model RSM turbulence approaches. We employ the two-equation standard κ-ε turbulence model incorporated with suitable wall functions. The interaction between chemistry and turbulence is taken into account using presumed-shape probability density functions PDFs. The radiation effects of the most important radiating species are taken into account supposing an optically-thin flame. This publication is aimed at implementing the physical influence upwinding scheme PIS for the estimation of the cell-face mixture fraction variance considering the physics of the reacting flows. We compare the accuracy of the current extended FEV-PIS formulation with the experimental data for prediction of the flame structure in terms of temperature, mean mixture fraction, species concentrations, and the root-mean-square RMS fluctuations of mixture fraction. Our results are in great agreement with those reported earlier by measurement.

Keywords**:** Detail chemistry, Flame holder, Bluff-body stabilized flame, Methanol turbulent nonpremixed flame, Finite element volume.

Nomenclature:

A	cell surface area
B_z	buoyant force
$\vec{e}$	coordinates of unit vector normal to the cell face
f, F	mixture fraction at integration point and node, respectively
f''^2, F''^2	mixture fraction variance at integration point and node, respectively
h, H	total enthalpy at integration point and node, respectively
n	total number of species
N	finite element shape function
p, P	pressure at integration point and node, respectively
r, z	radial and axial components in Cylindrical coordinates, respectively
R	gas constant
T	temperature
u, U	radial velocity components at integration point and node, respectively
v, V	axial velocity components at integration point and node, respectively
$\bar{V}$	total lagged velocity magnitude
$\vec{V}$	velocity vector
W	molecular weight
Y	mass fraction

ε, Ξ	turbulence dissipation rate at integration point and node, respectively	e	effective magnitude
κ, K	turbulence kinetic energy at integration point and node, respectively	i	cell face index
		ip	integration point
		j	finite element grid index
μ	molecular viscosity coefficient	m	chemical species index counter
ρ	mixture density	up	upwind point
χ	scalar dissipation rate	$\forall$	volume

Subscripts, Superscripts, and Accents

1. Introduction

Numerical methods are very helpful tools for studying the structure of bluff-body stabilized turbulent nonpremixed flames. In this regard, RSM turbulence approaches, i.e. κ-ε turbulence model, are well-known approaches for turbulence modeling; however, their empirical constants in the cylindrical frame need to be adjusted for correct prediction of recirculation zone, i.e. spreading rate, decay rate, and the length of the recirculation zone (Correa and Gulati, 1992; Dally et al., 1995). To surmount the closure problem of chemical source terms within these turbulence models, flamelet models are promising approaches using detailed chemical kinetics mechanisms (Peters, 1986).

Back to our past activities, we have already simulated an axisymmetric laminar nonpremixed flame using FEV method and fast chemistry approach (Darbandi et al., 2008). In fact, we extended the 2-D Cartesian PIS to the cylindrical frame application to calculate the conservation laws fluxes at the cell faces in laminar flow more accurately. We later extended our PIS formulation to turbulent flow applications (Darbandi et al., 2009). In this regard, we developed the PIS formulation to estimate the turbulence quantity fluxes at the cell faces. We simulated a turbulent nonpremixed flame using standard κ-ε turbulence model and the fast chemistry approach. We neglected the turbulence-chemistry interaction and radiation heat transfer of gas species mixture in our formulations and simulations.

In this work, we more extend our past FEV formulation to simulate a gaseous-methanol/air turbulent nonpremixed flame stabilized on an axisymmetric bluff-body burner considering a detailed chemistry. In this regard, we employ a detailed chemistry model containing 463 reversible chemical reactions between 70 chemical species. The interaction between chemistry and turbulence is taken into account using presumed-shape PDFs. We also utilize the flamelet model considering the mixture fraction variances. Bases on our past experiences in developing PIS formulations for cell-face flux calculations, we extend this scheme in terms of mixture faction variance benefiting from its transport equation. The radiation effects are taken into account assuming optically-thin gases. We compare our FEV-PIS formulations in terms of accuracy with accessible experimental data. A great agreement is found between the current numerical results and the measured data in terms of mean mixture fraction, temperature, species concentrations, and the RMS fluctuations of mixture fraction within the flame, i.e. the flame structure.

2. The Governing Equations

The fluid flow conservation laws consisting of continuity, *r*-momentum, and *z*-momentum are given by

$$\vec{\nabla}.\left(\rho\vec{V}\right) + \rho\frac{u}{r} = 0 \tag{1}$$

$$\vec{\nabla}.\left(\rho\vec{V}u\right) = -\frac{\partial p}{\partial r} + \vec{\nabla}\cdot\left(\mu_e\vec{\nabla}u\right) - \mu_e\frac{u}{r^2} + \frac{\mu_e}{r}\frac{\partial u}{\partial r} \tag{2}$$

$$\vec{\nabla}.\left(\rho\vec{V}v\right) = -\frac{\partial p}{\partial z} + \vec{\nabla}\cdot\left(\mu_e\vec{\nabla}v\right) + \frac{\mu_e}{r}\frac{\partial v}{\partial r} + B_z \tag{3}$$

Where $\mu_e = \mu+\mu_t$ and $B_z = -\rho g$. The transport equations for turbulence quantities are given by

$$\vec{\nabla}.\left(\rho\vec{V}\kappa\right) = \vec{\nabla}\cdot\left(\frac{\mu_e}{\sigma_\kappa}\vec{\nabla}\kappa\right) + \frac{\mu_e}{\sigma_\kappa r}\frac{\partial\kappa}{\partial r} + G_\kappa - \rho\varepsilon \quad (4)$$

$$\vec{\nabla}.\left(\rho\vec{V}\varepsilon\right) = \vec{\nabla}\cdot\left(\frac{\mu_e}{\sigma_\varepsilon}\vec{\nabla}\varepsilon\right) + \frac{\mu_e}{\sigma_\varepsilon r}\frac{\partial\varepsilon}{\partial r} + \frac{\varepsilon}{\kappa}(c_1 G_\kappa - c_2\rho\varepsilon) \quad (5)$$

where $G_\kappa=\mu_e\{2[(\partial v/\partial z)^2+(\partial u/\partial r)^2+(u/r)^2]+[(\partial v/\partial r)+(\partial u/\partial z)]^2\}$, $\mu_t=c_d\rho\kappa^2/\varepsilon$, σ_κ=0.9, σ_ε=1.22, c_1=1.44, c_2=1.84, and c_d=0.09 (Kent and Honerry, 1987). Apparently, wall function is a general idea to describe the flow behaviour near the solid walls due to dominant viscous effects there.

To model combustion in a turbulent diffusion flame, we use the flamelet model. The flamelet model takes into account the chemical nonequilibrium effects by introducing a new flow field parameter called scalar dissipation rate. It requires the solution of an additional transport equation for the variance of mixture fraction. Considering the flamelet combustion model, the intermediate species are taken into account via using the detailed chemical kinetics. In this study, we chose a detailed kinetic scheme which consists of 70 chemical species and 463 chemical reactions. Table 1 shows the list of implemented species.

Table. 1. Species taken into account in the current chemistry mechanism.

H_2	**H**	**O**	**O_2**	**OH**	**H_2O**	**HO_2**	**H_2O_2**	**C**
CH	**CH_2**	**CH_2^***	**CH_3**	**CH_4**	**CO**	**CO_2**	**HCO**	**CH_2O**
CH_2OH	**CH_3O**	**CH_3OH**	**C_2H**	**C_2H_2**	**C_2H_3**	**C_2H_4**	**C_2H_5**	**C_2H_6**
HCCO	**CH_2CO**	**HCCOH**	**AR**	**N_2**	**CH_2CHO**	**C_3H_2**	**C_3H_3**	**pC_3H_4**
aC_3H_4	**cC_3H_4**	**C_4H_2**	**H_2C_4O**	**n-C_4H_3**	**i-C_4H_3**	**C_4H_4**	**n-C_4H_5**	**i-C_4H_5**
C_4H_6	**C_4H_{612}**	**C_4H_{81}**	**C_4H_7**	**C_6H_2**	**C_6H_3**	**l-C_6H_4**	**c-C_6H_4**	**C_6H_6**
C_6H_5	**C_6H_5O**	**C_6H_5OH**	**C_5H_6**	**C_5H_5**	**C_5H_5O**	**C_5H_4OH**	**C_5H_4O**	**C_3H_8**
nC_3H_7	**iC_3H_7**	**C_3H_6**	**aC_3H_5**	**CH_3CCH_2**	**CH_3CHO**	**C_2H_3CHO**		

The transport equations for the first two moment of mixture fractions are given by

$$\vec{\nabla}.\left(\rho\vec{V}f\right) = \vec{\nabla}\cdot\left(\frac{\mu_e}{\sigma_f}\vec{\nabla}f\right) + \frac{\mu_e}{\sigma_f r}\frac{\partial f}{\partial r} \quad (6)$$

$$\vec{\nabla}.\left(\rho\vec{V}f''^2\right) = \vec{\nabla}\cdot\left(\frac{\mu_e}{\sigma_f}\vec{\nabla}f''^2\right) + \frac{\mu_e}{\sigma_f r}\frac{\partial f''^2}{\partial r} + c_g\mu_e\left(\vec{\nabla}f\right)^2 - \rho c_\chi\frac{\varepsilon}{\kappa}f''^2 \quad (7)$$

Where c_g=2.86 and c_χ=2. The scalar dissipation rate can be calculated from $\chi=c_\chi f''^2\varepsilon/\kappa$. On the other hand, the laminar flamelets are modeled as an opposed diffusion flow using the scalar dissipation rate. The turbulence-chemistry interaction is taken into account using the probability density functions PDFs, i.e. the β function and a log-normal function. The results from pre-computed laminar flamelets and turbulent statistics can be tabulated as a three-dimensional lookup table such that all thermo-chemical quantities can be obtained from the calculated mean mixture fraction, variance of mixture fraction, and scalar dissipation rate over the solution domain (Suzer et al., 2010).

Assuming a unit Lewis number, the enthalpy equation is given by

$$\vec{\nabla}.\left(\rho\vec{V}h\right) = \vec{\nabla}\cdot\left(\frac{\mu_e}{\sigma_h}\vec{\nabla}h\right) + \frac{\mu_e}{\sigma_h r}\frac{\partial h}{\partial r} + q_{rad} \quad (8)$$

In which the turbulent Prandtl/Schmidt numbers, σ_h and σ_f, are assumed to be 0.85. Thermal radiation of gases is taken into account assuming an optically thin flame. Finally, the density is obtained from the equation of state as $p = \rho RT \sum_{m=1}^{n} Y_m/W_m$.

3. Domain Discretization and Computational Modelling

To apply the FEV method, the solution domain should be discretized into a large number of elements. Figure 1 shows a part of the solution domain. The current elements' shape is quadrilateral. Element nodes, shown by circles in Figure 1, are the locations of unknown flow variables. As is seen in this figure, each element is broken into four quadrilateral sub-elements. They are shown by dashed lines. Each four surrounding sub-elements, which enclose one node, is known as the control volume or cell. It is shown by the shaded area in Figure 1. The discretized governing equations are integrated over all control volumes. In other words, the employment of Gauss divergence theorem to Eqs. (1)-(8) and benefiting from the summation symbol to indicate the integration over the entire cell faces of one control volume, we arrive to

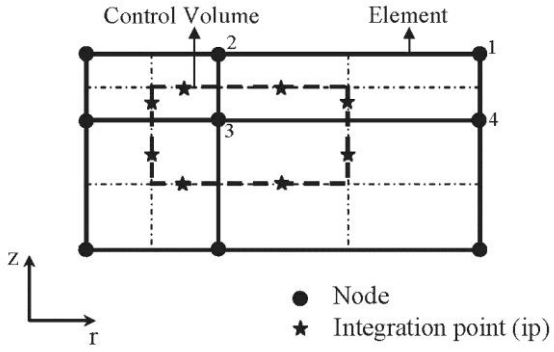

Fig. 1. A part of the solution domain illustrating four elements, one complete finite volume, sixteen sub-volumes, and eight cell faces.

$$\sum_{i=1}^{ns}[\rho(u\,dA_r + v\,dA_z)]_i = -\int_{\forall} \rho\frac{u}{r}d\forall \tag{9}$$

$$\sum_{i=1}^{ns}[\rho\bar{u}\,u\,dA_r + \rho\bar{v}\,u\,dA_z]_i = -\sum_{i=1}^{ns}(p dA_r)_i + \sum_{i=1}^{ns}\left[\mu_e\left(\frac{\partial u}{\partial r}dA_r + \frac{\partial u}{\partial z}\,dA_z\right)\right]_i + \int_{\forall} \mu_e\left(\frac{1}{r}\frac{\partial u}{\partial r} - \frac{u}{r^2}\right)d\forall \tag{10}$$

$$\sum_{i=1}^{ns}[\rho\bar{u}\,v\,dA_r + \rho\bar{v}\,v\,dA_z]_i = -\sum_{i=1}^{ns}(p dA_z)_i + \sum_{i=1}^{ns}\left[\mu_e\left(\frac{\partial v}{\partial r}dA_r + \frac{\partial v}{\partial z}\,dA_z\right)\right]_i + \int_{\forall} \mu_e\frac{1}{r}\frac{\partial v}{\partial r}d\forall + \int_{\forall} B_z d\forall \tag{11}$$

$$\sum_{i=1}^{ns}[\rho\bar{u}\,\kappa\,dA_r + \rho\bar{v}\,\kappa\,dA_z]_i = \sum_{i=1}^{ns}\left[\frac{\mu_e}{\sigma_\kappa}\left(\frac{\partial \kappa}{\partial r}dA_r + \frac{\partial \kappa}{\partial z}\,dA_z\right)\right]_i + \int_{\forall} \frac{\mu_e}{\sigma_\kappa}\frac{1}{r}\frac{\partial \kappa}{\partial r}d\forall + \int_{\forall} (G_\kappa - \rho\varepsilon)d\forall \tag{12}$$

$$\sum_{i=1}^{ns}[\rho\bar{u}\,\varepsilon\,dA_r + \rho\bar{v}\,\varepsilon\,dA_z]_i = \sum_{i=1}^{ns}\left[\frac{\mu_e}{\sigma_\varepsilon}\left(\frac{\partial \varepsilon}{\partial r}dA_r + \frac{\partial \varepsilon}{\partial z}\,dA_z\right)\right]_i + \int_{\forall} \frac{\mu_e}{\sigma_\varepsilon}\frac{1}{r}\frac{\partial \varepsilon}{\partial r}d\forall + \int_{\forall} \frac{\varepsilon}{\kappa}(c_1 G_\kappa - c_2\rho\varepsilon)d\forall \tag{13}$$

$$\sum_{i=1}^{ns}[\rho\bar{u}\,f\,dA_r + \rho\bar{v}\,f\,dA_z]_i = \sum_{i=1}^{ns}\left[\frac{\mu_e}{\sigma_f}\left(\frac{\partial f}{\partial r}dA_r + \frac{\partial f}{\partial z}\,dA_z\right)\right]_i + \int_{\forall} \frac{\mu_e}{\sigma_f}\frac{1}{r}\frac{\partial f}{\partial r}d\forall \tag{14}$$

$$\sum_{i=1}^{ns}[\rho\bar{u}\,f"^2\,dA_r + \rho\bar{v}\,f"^2\,dA_z]_i = \sum_{i=1}^{ns}\left[\frac{\mu_e}{\sigma_f}\left(\frac{\partial f"^2}{\partial r}dA_r + \frac{\partial f"^2}{\partial z}\,dA_z\right)\right]_i + \int_{\forall} \frac{\mu_e}{\sigma_f}\frac{1}{r}\frac{\partial f"^2}{\partial r}d\forall + \int_{\forall} \left[c_g\mu_e\left(\vec{\nabla}f\right)^2 - \rho c_\chi\frac{\varepsilon}{\kappa}f"^2\right]d\forall \tag{15}$$

$$\sum_{i=1}^{ns}[\rho\bar{u}\ h\ dA_r + \rho\bar{v}\ h\ dA_z]_i = \sum_{i=1}^{ns}\left[\frac{\mu_e}{\sigma_h}\left(\frac{\partial h}{\partial r}dA_r + \frac{\partial h}{\partial z}\ dA_z\right)\right]_i + \int_{\forall}\ \frac{\mu_e}{\sigma_h}\frac{1}{r}\frac{\partial h}{\partial r}d\forall + \int_{\forall}\ q_{rad}d\forall \quad (16)$$

Where $\overrightarrow{dA} = dA_r\overrightarrow{e_r} + dA_z\overrightarrow{e_z}$ is the normal vector to each cell face and *i* counts the number of cell faces. The nonlinear convection terms are linearized using the known velocity components from the previous iteration. They are indicated by an overbar. Due to the elliptic nature of pressure terms in the momentum equations and the diffusion terms in all of the transport equations, they can be estimated at the cell faces using the FE shape functions. In other words, using the FE shape functions, we can provide suitable relations between the parameter magnitude at the cell face, denoted by lower case letters, and their nodal magnitudes denoted by upper case letters. This treatment results in

$$p_i = \sum_{j=1}^{4}\ N_{ij}P_j\ ,\ (\partial\phi/\partial\xi)_i = \sum_{j=1}^{4}\left(\partial N_j/\partial\xi\right)_i\Phi_j \quad (17)$$

Where *i* and *j* count the face numbers for a cell and the node numbers for an element, respectively. Additionally, the variable ξ represents either *r* or *z* coordinates. Moreover, ϕ (and Φ) represents *u* (and *U*), *v* (and *V*), κ (and *K*), ε (and Ξ), *f* (and *F*), f''^2 (and F''^2), and *h* (and *H*). Important care should be given to the left hand side of the discretized transport equations, i.e. Eqs. (9)-(16). Indeed, the advection terms would have different nature than the pressure and diffusion terms. In other words, these terms mostly need to be treated using upwind-biased schemes. Therefore, the current authors extended an upwind-base scheme (PIS) to respect the physical behaviour of advection terms in the current governing equations. The results of this scheme, which can be derived from an arbitrary transport equation, can be utilized to estimate the advection fluxes of its transported quantity. Using the PIS scheme in a cylindrical frame, the cell face parameters are given by

$$u_{ipi} = \left(\frac{Q_1}{Q} + \frac{Q_2}{Q} + \frac{Q_3}{Q} - \frac{Q_4}{Q}\right)_{ipi}U_j + \left(-\frac{Q_5}{Q}\sum_{j=1}^{4}\frac{\partial N_j}{\partial r}\right)_{ipi}P_j \quad (18)$$

$$v_{ipi} = \left(\frac{Q_1}{Q} + \frac{Q_2}{Q} + \frac{Q_3}{Q}\right)_{ipi}V_j + \left(-\frac{Q_5}{Q}\sum_{j=1}^{4}\frac{\partial N_j}{\partial z}\right)_{ipi}P_j + \left(\frac{Q_5}{Q}B_z\right)_{ipi} \quad (19)$$

$$\kappa_{ipi} = \left(\frac{Q_1}{Q_\kappa} + \frac{Q_2}{\sigma_\kappa Q_\kappa} + \frac{Q_3}{\sigma_\kappa Q_\kappa}\right)_{ipi}K_j + \left(\frac{Q_5}{Q_\kappa}(G_\kappa - \rho\varepsilon)\right)_{ipi} \quad (20)$$

$$\varepsilon_{ipi} = \left(\frac{Q_1}{Q_\varepsilon} + \frac{Q_2}{\sigma_\varepsilon Q_\varepsilon} + \frac{Q_3}{\sigma_\varepsilon Q_\varepsilon}\right)_{ipi}\Xi_j + \left(\frac{Q_5}{Q_\varepsilon}\frac{\varepsilon}{\kappa}(c_1G_\kappa - c_2\rho\varepsilon)\right)_{ipi} \quad (21)$$

$$f_{ipi} = \left(\frac{Q_1}{Q_f} + \frac{Q_2}{\sigma_f Q_f} + \frac{Q_3}{\sigma_f Q_f}\right)_{ipi}F_j \quad (22)$$

$$f''^2_{ipi} = \left(\frac{Q_1}{Q_f} + \frac{Q_2}{\sigma_f Q_f} + \frac{Q_3}{\sigma_f Q_f}\right)_{ipi}F''^2_j + \left(\frac{Q_5}{Q_f}\left(2\frac{\mu_e}{\sigma_f}\left(\vec{\nabla}f\right)^2 - \rho c_\chi\frac{\varepsilon}{\kappa}f''^2\right)\right)_{ipi} \quad (23)$$

$$h_{ipi} = \left(\frac{Q_1}{Q_h} + \frac{Q_2}{\sigma_h Q_h} + \frac{Q_3}{\sigma_h Q_h}\right)_{ipi}H_j + \left(\frac{Q_5}{Q_h}q_{rad}\right)_{ipi} \quad (24)$$

where $Q_1 = \rho|V|L_d^2\sum_{j=1}^{4}N_{j_{up}}$, $Q_2 = \mu_e L_c\sum_{j=1}^{4}N_j$, $Q_3 = (\mu_e/r)L_cL_d^2\sum_{j=1}^{4}\left(\partial N_j/\partial r\right)$, $Q_4 = (\mu_e/r^2)L_cL_d^2\sum_{j=1}^{4}N_j$, $Q_5 = L_cL_d^2$, $Q = \rho|V|L_d^2 + \mu_e L_c$, $Q_\kappa = \rho|V|L_d^2 + (\mu_e/\sigma_\kappa)L_c$, $Q_\varepsilon = \rho|V|L_d^2 +$

$(\mu_e/\sigma_\varepsilon)L_c$, $Q_\varepsilon = \rho|V|L_d^2 + (\mu_e/\sigma_\varepsilon)L_c$, $Q_f = \rho|V|L_d^2 + (\mu_e/\sigma_f)L_c$, and $Q_h = \rho|V|L_d^2 + (\mu_e/\sigma_h)L_c$.

Additionally, L_c and L_d are the convection and diffusion length scales, respectively.

As is observed in Eqs. (18)-(24), each cell face parameter can be related to its nodal magnitudes at the same element via applying the PIS scheme. The substitution of Eqs. (18)-(19) in Eqs. (9)-(11), it results in a stiffness matrix for a cell and eventually many cell stiffness matrices for the entire cells. Due to direct appearances of pressure and the two velocity components in each cell conservation law, a strong coupling is established between the main unknowns in the current formulations, See Eqs. (18)-(19). In other words, the pressure-velocity decoupling or the checkerboard problem is resolved automatically here. These cell stiffness matrices can be assembled properly in the next stage to construct a global stiffness matrix. Some more numerical considerations are required to solve the achieved sparse matrix efficiently. In a similar manner, the substitutions of Eqs. (20)-(24) in Eqs. (12)-(16) will result in another set of algebraic equations, which should be solved using proper algebraic matrix solver algorithms (Darbandi et al., 2006, 2008; Vakili and Darbandi, 2009). Using a bi-implicit algorithm, the latter set of algebraic equations are solved separately using the former strategy.

4. The Test Case

A gaseous-methanol/air turbulent nonpremixed flame stabilized on an axisymmetric bluff-body burner is chosen to verify the achieved numerical solutions. We employ the experimental conditions of Dally et al. (1998) to perform our simulations. Figure 2 shows the configuration of the bluff-body burner. Because of the symmetry of problem, we consider a rectangular solution domain applying the symmetry boundary conditions at the centre line. The computational domain has 0.1 m × 0.7 m dimensions, i.e. R_0=0.1 m, and L=0.7 m, see Fig. 2. The burner has a bluff-body diameter, D_B=50 mm, i.e. R_B=25 mm. The fuel nozzle diameter is 3.6 mm, i.e. R_1=1.8 mm. This fuel nozzle injects the pure gaseous methanol as the fuel at a speed of 121 m/s into the combustor. The oxidizer, i.e. co-flow air stream, which consists of 23.3 ٪oxygen and 76.7 ٪nitrogen, enters the combustor at a speed of 40 m/s. The initial temperatures of methanol and air are 373 K and 300 K, respectively. As is understood, the methanol is evaporated and delivered through a heated line and injected into the combustion chamber.

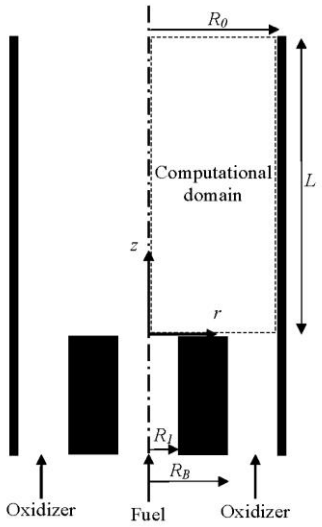

Fig. 2. The configuration of the O-ring-type flame holder in a combustion chamber (Dally et al., 1998).

5. The Results

To simulate the bluff-body stabilized methanol/air turbulent nonpremixed flame in a combustor, we broke the computational domain into a huge number of quadrilateral elements. Using uniform grid

distribution, the elements' sizes are 0.5 mm and 0.5 mm in the radial and axial directions, respectively. To evaluate the accuracy of our new developed formulations, we solve the test case given in Dally et al. (1998). Therefore, we can compare the predicted flame structure, i.e. the distributions of mixture fraction, species concentrations, temperature, and the RMS of mixture fraction within the flame with the data collected by this reference.

Figure 3 presents the distributions of mean mixture fraction, temperature, OH mass fraction, and mixture fraction RMS at two axial locations of z/D_B=0.26 and 1.30 downstream of bluff-body burner. The figure shows that there are great agreements with the data reported by Dally et al. (1998). As is seen, our numerical results accurately predict the flame length and envelop.

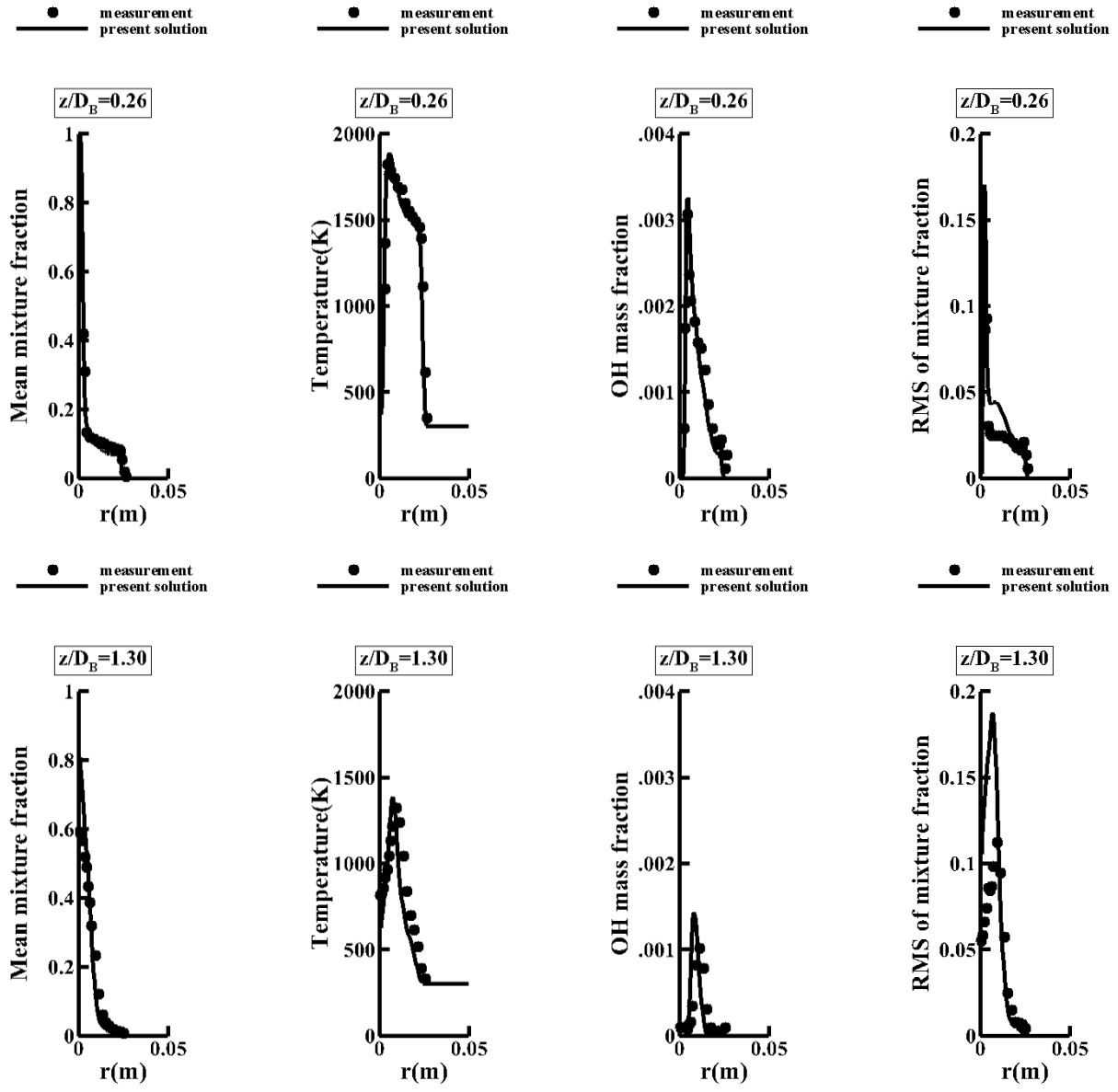

Fig. 3. The current radial distribution of mean mixture fraction, temperature, OH mass fraction, and mixture fraction RMS in a bluff-body stabilized methanol/air turbulent nonpremixed flame and comparison with the data collected by Dally et al. (1998).

6. Conclusion

A bluff-body stabilized gaseous-methanol/air turbulent nonpremixed flame was simulated in a combustor using a detailed chemistry. We utilized flamelet combustion model within the RSM turbulence approach. We adopted a chemical scheme with 463 reversible chemical reactions between 70 chemical species. The interaction between chemistry and turbulence was taken into account using the presumed-shape PDFs. We employed the two-equation standard κ-ε turbulence model incorporated with suitable wall functions. Supposing optically-thin gases, the gaseous-mixture radiation effects are taken into account. The nonequilibrium effects of turbulence are considered thorough the calculations of mixture fraction variance. Benefiting from our past experiences in the calculation of cell-face fluxes, we chose the FEV method and more extended the PIS scheme in terms of mixture fraction variance. As our test case, we solved a gaseous-methanol/air turbulent nonpremixed flame stabilized on an axisymmetric bluff-body burner. We compared our results in terms of the distributions of mean mixture fraction, temperature, species concentrations, and the RMS fluctuations of mixture fraction within the flame. The present results showed that there are great agreements with the measured data. It is found that the current FEV-PIS formulations can accurately predict the structure of a bluff-body stabilized methanol/air turbulent nonpremixed flame.

Acknowledgements

The authors would like to thank the financial support received from the Deputy of Research and Technology in Sharif University of Technology. Their financial support and help are greatly acknowledged.

References

Correa S. M., Gulati A. (1992). Measurements and modeling of a bluff body stabilized flame, *Combust. Flame*, 89, 195–213.

Dally B. B., Fletcher D. F., Masri A. R. (1995). Computations of a non-reacting bluff body jet flow, *Proc. First Asian CFD Conference*, Hong Kong, 177–182.

Dally B. B., Masri A. R., Barlow R. S., Fiechtner G. J. (1998). Instantaneous and Mean Compositional Structure of Bluff-Body Stabilized Nonpremixed Flames, *Combust. Flame*, 114, 119–148.

Dally B. B., Masri A. R., Fletcher D. F. (1995). Modelling of Bluff-Body Recirculating Flows, *Twelfth Australasian Fluid Mechanics Conference*, Sydney, Australia, 1, 529–532.

Darbandi M., Ghafourizadeh M., Schneider G.E. (2008). Developing a novel FEV formulation to solve laminar diffusive flame in the cylindrical coordinates, *The 46th AIAA Aerospace Sciences Meeting and Exhibit*, Reno, Nevada, AIAA 2008–1257.

Darbandi M., Ghafourizadeh M., Schneider G.E. (2009). Numerical calculation of turbulent reacting flow in a model gas-turbine combustor, *41st AIAA Thermophysics Conference*, San Antonio, Texas, AIAA 2009–3926.

Darbandi M., Schneider G. E., Vakili S. (2006). Using Different Preconditioned Krylov Subspace Methods to Solve Coupled Fluid Flow Equations, *CFD J.*, 15, 35–43.

Darbandi M., Vakili S., Schneider G. E. (2008). Efficient Multilevel Restriction-Prolongation Expressions for Hybrid Finite Volume Element Method, *Inter. J. CFD*, 22, 29–38.

Kent J. H., Honnery D. (1987). Soot and Mixture Fraction in Turbulent Diffusion Flames, *Combustion Science and Technology*, 54, 383-397.

Peters N. (1986). Laminar Flamelet Concepts in turbulent combustion, *Twenty-First Symposium (International) on Combustion, The Combustion Institute*, Pittsburgh, 1231–1250.

Suzer E., Hassan E. A., Yun S., Thakur S., Wright J., Ihme M., Shyy W. (2010). Turbulence-Chemistry Interaction and Heat Transfer Modeling of H2/O2 Gaseous Injector Flows, *48th AIAA Aerospace Sciences Meeting Including the New Horizons Forum and Aerospace Exposition*, AIAA 2010–1525.

Vakili S., Darbandi M. (2009). Recommendations on Enhancing the efficiency of Algebraic Multigrid Preconditioned GMRES in Solving Coupled Fluid Flow Equations, *Numer. Heat Transfer*, 55, 232–256.